ADVANCED FUNCTIONAL MATERIALS
www.afm-journal.de

Ferroelectric Modulation of ReS_2-Based Multifunctional Optoelectronic Neuromorphic Devices for Wavelength-Selective Artificial Visual System

*Zhaoying Dang, Feng Guo, Yifei Zhao, Kui Jin, Wenjing Jie, and Jianhua Hao**

Neuromorphic optoelectronic vision system inspired by the biological platform displays potential for in-sensor computing. However, it is still challenge to process multiwavelength image in noisy environment with simple device configuration and light-tunable biological plasticity. Here, a prototype visual sensor is demonstrated based on ferroelectric copolymer poly(vinylidene fluoride-trifluoroethylene) (P(VDF-TrFE)) and 2D rhenium disulfide (ReS_2) with integration of recognition, memorization, and pre-processing functions in the same device. Such synaptic devices achieve impressive electronic characteristics, including a current on/off ratio of 10^9 and mobility of 45 $cm^2 V^{-1} s^{-1}$. Various synaptic plasticity behaviors have been achieved owing to the switchable ferroelectricity, enabling them to establish an artificial neural network (ANN) with high digit recognition accuracy of 89%. Through constructing optoelectronic device array, object extraction is achieved with wavelength-selective capability in noisy environment, closely resembling human retina for color recognition. Above outcomes bring a notable improvement in the image recognition rate from 72% to 96%. Besides, low energy consumption comparable to single biological event can be realized. With these multifunctional features, this work inspires highly integrated neuromorphic systems and the development of wavelength-selective artificial visual platform.

1. Introduction

Human visual system, consisting of the retina, optic nerve, and visual cortex, plays a crucial role in acquiring and filtering information from the external world with remarkable real-time perception and visual information processing abilities.[1] Compared to the traditional machine vision system based on von Neumann architecture, the bio-inspired neuromorphic vision systems can integrate features of the sensing, memory and processing.[2–5] Researchers have currently made progress in developing 2D materials-based visual devices that closely replicate the functions of various cells in the human visual system.[6–8] These innovative devices are capable of detecting and processing visual information[9,10] and have also achieved the improved recognition accuracy.[11–14] Such synaptic devices contribute to the integration and energy-saving for computation architecture.[15,16]

One of the crucial functionalities of the retinal cell is the ability to discern colorful information while extracting relevant signals from the noisy environment, resembling the process involved in conducting color blindness screening tests. Also, by leveraging the color-recognition mechanism, extracting crucial light information can effectively reduce interference caused by redundant data and enhance the speed of next signal processing. This characteristic closely aligns with the efficient information processing observed in the human visual system.[17,18] However, it is still challenging to achieve such complicated sensing or learning purposes based on one simple optoelectronic synaptic device. In this regard, channel materials with higher performance, more simplified structures, and adjustable device mechanisms need to be investigated for

Z. Dang, F. Guo, Y. Zhao, J. Hao
Department of Applied Physics
The Hong Kong Polytechnic University
Hong Kong 999077, China
E-mail: jh.hao@polyu.edu.hk

The ORCID identification number(s) for the author(s) of this article can be found under https://doi.org/10.1002/adfm.202400105

DOI: 10.1002/adfm.202400105

Z. Dang, K. Jin
Songshan Lake Materials Laboratory
Dongguan, Guangdong 523808, China

Z. Dang, F. Guo, J. Hao
The Hong Kong Polytechnic University Shenzhen Research Institute
Shenzhen, Guangdong 518057, China

W. Jie
College of Chemistry and Materials Science
Sichuan Normal University
Chengdu, Sichuan 610066, China

J. Hao
Research Centre for Nanoscience and Nanotechnology
The Hong Kong Polytechnic University
Hong Kong 999077, China

multifunctional neuromorphic visual platform. Combination of 2D direct bandgap materials and ferroelectric materials as heterostructures holds potential for neuromorphic visual sensors.[19,20] ReS_2 is adopted as channel layer for several reasons. 1) It manifests a direct bandgap over a broad range of thicknesses.[21] 2) ReS_2 demonstrates remarkable stability and enhanced light absorption capabilities, making it a promising candidate for optoelectronic applications.[22] 3) ReS_2 exhibits weak interlayer coupling and a low energy barrier for sulfur vacancy formation. Thus, the activation barrier experienced by electrons trapped at sulfur vacancies hinders radiative recombination[23–25] and the pronounced persistent photoconductivity effect (PPC) is more likely to be observed. On the other hand, the transparent ferroelectric copolymer P(VDF-TrFE) is used as dielectrics, allowing for efficient light transmission. The low-temperature spin-coating process compared with traditional ferroelectric materials facilitates the formation of a good van der Waals (vdWs) interface between the semiconductor and ferroelectric copolymer.[26,27] Furthermore, ferroelectric copolymers exhibit exceptional mechanical stability and flexibility, making them highly suitable for thin film fabrication at comparatively low temperatures on various flexible substrates with cost-effective processing techniques.[28,29]

In this work, we design a multifunctional optoelectronic ferroelectric synaptic transistor consisting of 2D materials ReS_2 and ferroelectric polymer P(VDF-TrFE) with the simultaneous synapse behaviors simulation, multi-color perception, and visual neuromorphic computing functionalities. The comprehensive study includes detailed optoelectronic performances and mixed-wavelength image preprocessing pertaining to basic synapse plasticity. Versatile synaptic behaviors, including paired-pulse facilitation (PPF), short-term/long-term potentiation (STP/LTP), short-term memory (STM) and long-term memory (LTM) transition can be realized. Advanced neuromorphic feature of learning-forgetting-relearning process is also successfully mimicked. Based on single optoelectronic synapse, we establish a neuromorphic visual array model to simulate the retina for light-intensity sensing and color distinguishment. Through light-induced conductance difference, the contrast of the desired object becomes more obvious while reducing surrounding noise signals. The optoelectronic devices array is trained to implement image recognition with a high accuracy of 96%. These findings demonstrate the potential of the ferroelectric optoelectronic device to achieve perception, object recognition, and energy-efficient operations, bringing one step closer to replicating the human visual system.

2. Results and Discussion

In **Figure 1**a, an illustration of the biological human visual system is presented, highlighting the three essential steps in vision information processing. Initially, optical signals are converted into electrical signals by the retina. The rod and cone photoreceptors play distinct roles in detecting light intensity and light colors, respectively.[30] Subsequently, these electrical signals travel through the optic nerves, reaching the visual cortex where visual features are extracted. Ultimately, visual features are transmitted to higher brain regions for cognitive processes.[31] Motivated by the diverse functionalities of the human vision system, three-terminal ferroelectric synaptic transistor is proposed to emulate the retina in terms of multi-wavelength sensing, electrical signal conversion, and image information processing.[32] The receptors on the postsynaptic neuron receive the external stimulus released from the presynaptic neurons through the diffusion effect of neurotransmitters. This process allows for the modulation of the strength and magnitude of the postsynaptic response, thereby reflecting synaptic plasticity.[33] The detailed synaptic device structure including P(VDF-TrFE) and ReS_2 is displayed in Figure 1b, which is regulated by optical and electrical signals.

Exfoliated ReS_2 flakes are carefully selected as channel material for its inherent photoresponsivity property. Ferroelectric polymer P(VDF-TrFE) is spin-coated onto the ReS_2 to create a top-gate architecture. More details about device fabrication process can be found in Figure S1 (Supporting Information) and the method section. In Figure 1b, the molecular chain configuration of P(VDF-TrFE) and the crystal structure of ReS_2 are provided. The Raman spectrum of ReS_2 in Figure 1c shows characteristic peaks of A_g-type modes, located at 138 and 143 cm^{-1}, and E_g-type modes, located at 152, 162, 212 cm^{-1}. A_g mode and E_g mode correspond to the out-of-plane and in-plane vibrational modes of the Re atoms, respectively.[34] Other remaining higher-frequency Raman peaks originate from the vibration modes of lighter S atoms (Figure S2, Supporting Information). The thickness of ReS_2 is ≈8 nm measured by atomic force microscopy (AFM) (Figure S3, Supporting Information). The β phase of P(VDF-TrFE) confirmed by X-ray diffraction (XRD) has the largest spontaneous polarization (Figure S4, Supporting Information). This phase is characterized by the alignment of molecular chains in the same direction, resulting in a high dipole moment due to the distribution of positively charged hydrogen atoms and negatively charged fluorine atoms.[35] The coercive voltage (V_c) is determined to be 15 V and the remnant polarization (P_r) is 6 μC cm^{-2}, as shown in Figure 1d. Furthermore, the abrupt changes observed in the parallelogram-shaped piezoelectric response loops and butterfly-shaped amplitude loops indicate that the polarization is compelled to shift upwards or downwards under the influence of the applied writing voltage (Figure 1e). By applying voltage with opposite polarity, the ferroelectric domains exhibit distinct phase differences, suggesting the stability to program the ferroelectric domains into arbitrary shapes (Figure 1f).[36]

Electrical tunable synaptic plasticity is crucial for signal conversion and lays the foundation for information extraction reflected by post-synaptic current (PSC). All electrical characterizations are carried out in vacuum at room temperature. In **Figure 2**a, a series of output curves ranging from 10 V to 25 V with a step of 5 V are presented. These output characteristics exhibit a linear correlation within a bias voltage range of −1 to 1 V, suggesting an Ohmic contact between the ReS_2 channel and Au electrodes. Subsequently, transfer curves of P(VDF-TrFE)/ReS_2 transistors are examined (Figure 2b). The ferroelectric field effect transistors based on multilayer ReS_2 possess high current ratios of up to 10^9 between on and off states, suggesting a high-quality interface between ReS_2 and P(VDF-TrFE) and the effective ferroelectric modulation for the ReS_2 channel.[37] Gate current is shown in the Figure S5 (Supporting Information). The measured transfer characteristics also exhibit a typical n-type behavior and a large memory window (≈14 V) during the hysteresis process, which is related to the nonvolatile ferroelectric polarization. Conversely, the ReS_2 device on a silicon substrate without ferroelectric

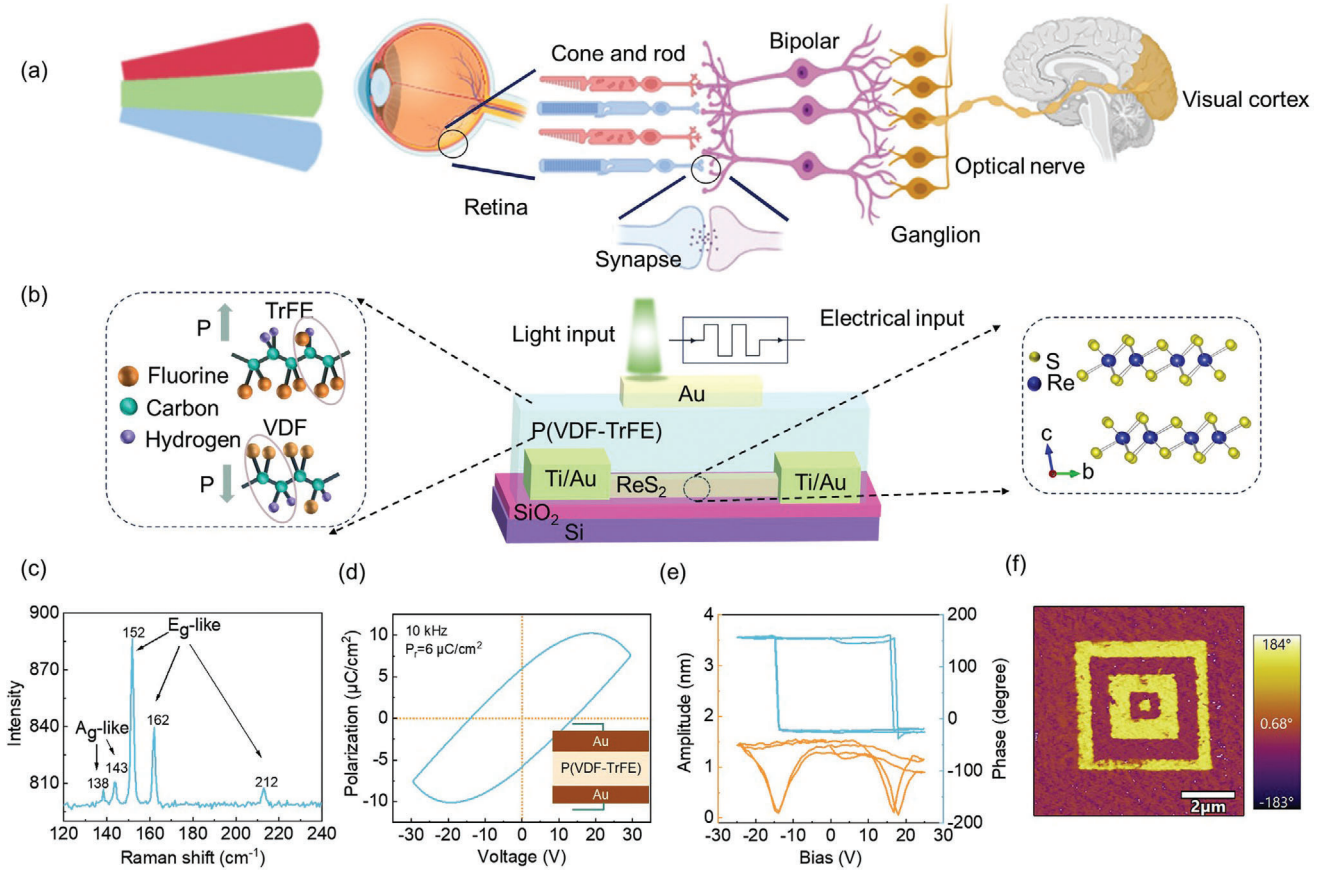

Figure 1. Human visual system and characterization of three-terminal ferroelectric synaptic devices. a) Schematic illustration of biological vision system including the retina, optical nerve, and visual cortex as well as a basic component of one synapse. b) 3D structure of artificial optoelectronic synapse based on P(VDF-TrFE) and ReS_2. c) The Raman spectrum of ReS_2 nanosheet. d) Ferroelectric hysteresis loop acquired in Au-P(VDF-TrFE)-Au capacitor at a test frequency of 10 kHz. e) The hysteresis loops of PFM phase and amplitude observed in P(VDF-TrFE). f) The PFM phase of P(VDF-TrFE) after being polarized by probes, demonstrating a "box-in-box" ferroelectric domain pattern.

gating does not exhibit a hysteresis window for both transfer and output characteristics, as shown in Figure S6 (Supporting Information), indicating that ferroelectric polarization plays a dominant role in tuning the electronic behavior of the channel. In the linear scale of the transfer curve, the hysteresis window becomes larger as the gate voltage range increases (Figure S7, Supporting Information). Moreover, the linear mobility is plotted (Figure 2c) and the mobility calculation process is shown in Note S1 (Supporting Information). The mobility values span a range of 40 to 45 $cm^2\ V^{-1}\ s^{-1}$ across all gate voltages. Therefore, it is worthwhile to mention that the electrical performance of P(VDF-TrFE)/ReS_2 devices are reasonably superior in terms of on/off ratio and carrier mobility.[38,39]

The above performances confirm that the prepared devices possess nonvolatile ferroelectric behaviors and the fundamental potential to emulate biological synaptic plasticity. Next, the synaptic behaviors based on a single electrical pulse are investigated. As shown in Figure 2d, excitatory postsynaptic current (EPSC) responses are triggered by the gate voltage with amplitude from 10 V to 25 V while maintaining a constant pulse duration time of 0.1 s. Increasing the pulse amplitude leads to higher EPSC. Additionally, following stimulation with voltage pulses, the EPSCs do not return to their initial values, and a higher voltage amplitude will bring a noticeable remaining current. This observation indicates a transition from short-term potentiation to long-term potentiation through voltage amplitude adjustment. Moreover, the pulse width also demonstrates effective modulation of the channel current. The EPSC gradually increases with an increase in pulse width, while the EPSC decay is slower for longer pulse widths (Figure S8, Supporting Information). Hence, larger amplitude and longer width are conducive to ferroelectric polarization, confirming a correlation between ferroelectric nonvolatility and EPSC modulation. Furthermore, we investigate the response speed of P(VDF-TrFE)/ReS_2 devices. The devices exhibit a response time of 2 ms when subjected to 20 V and -20 V write spikes, as illustrated in Figure S9 (Supporting Information).

It is widely recognized that short-term synaptic plasticity plays a pivotal role in information processing and the human brain memory, and it primarily involves paired-pulse facilitation (PPF) and paired-pulse depression (PPD) phenomena.[40] As illustrated in the inset of Figure 2e, the emulation of PPF behavior is achieved by delivering a pair of pre-synaptic pulses (20 V, 100 ms) to the device. In this context, A1 and A2 denote the peak values of the current of the first and second pulse, respectively. Notably, the

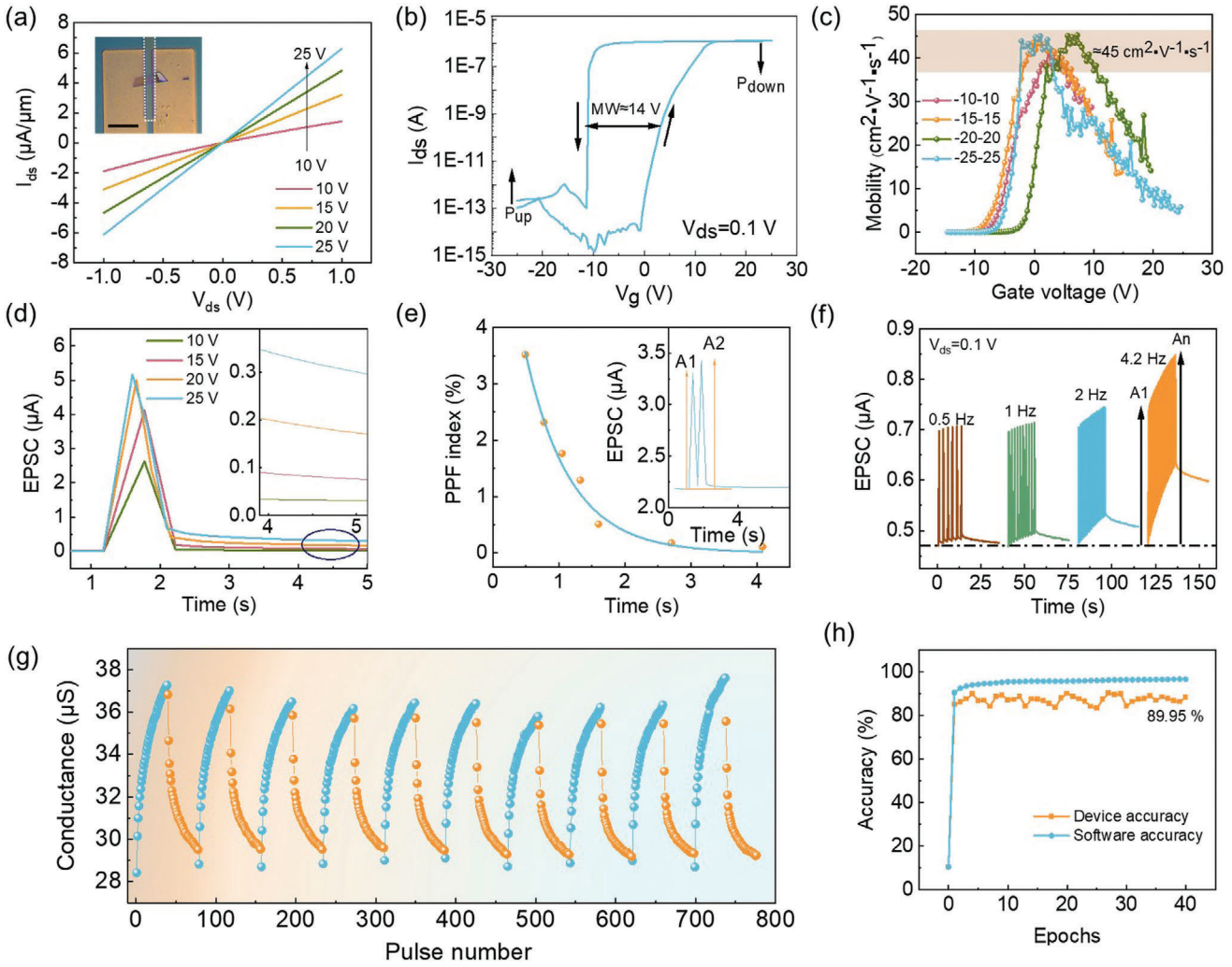

Figure 2. Electronic performances of the P(VDF-TrFE)/ReS_2 artificial synapse. a) Output characteristics under various top gate voltages, indicating excellent linearity in the range of −1–1 V. b) Transfer curve at V_{ds} of 0.1 V, demonstrating ferroelectric hysteresis behavior. c) Linear mobility plot of top gate P(VDF-TrFE)/ReS_2 transistors. d) EPSC behaviors are triggered by a single electrical spike with different pulse amplitude (from 10 V to 25 V) under 0.1 s pulse width, realizing the transition from short-term potentiation to long-term potentiation. e) PPF index change with pulse interval time. The inset is EPSC triggered by two consecutive electrical pulses with an interval time of 100 ms. f) EPSC responses depend on the frequency of electric spikes. g) Process of synaptic potentiation and depression by applying successive gate voltage spikes ($V_g = \pm 20$ V $t_{on} = 100$ ms). h) Accuracy of handwritten digit recognition based on LTP/LTD processes.

EPSC elicited by the second pulse surpasses that of the first pulse, successfully simulating the PPF behavior. Subsequently, the relationship between the synaptic weights and the interval time can be analyzed by varying the interval time of the two pulses. The PPF index, depicted in Figure 2e, can be mathematically expressed with Equation (1) and fitted by exponential decay function (2):

$$PPF\ index = \frac{A_2 - A_1}{A_1} \times 100\% \quad (1)$$

$$y = C_0 + C_1 e^{\frac{-x_1}{t_1}} + C_2 e^{\frac{-x_1}{t_2}} \quad (2)$$

Parameters t_1 (67.88 ms) and t_2 (718 ms) represent the fast and slow relaxation processes, respectively, which are consistent with biological synapses in the range of milliseconds. C_0 represents a constant value of zero, indicating that the ratio of the PPF gradually approaches zero. Whereas C_1 and C_2 refer to the initial magnitudes of the two aforementioned phases.[41,42] The fitting curve demonstrates that the synaptic weights can be significantly improved by decreasing the interval time between the two consecutive pulses. When the interval time becomes sufficiently large, the EPSC reaches a saturation level and remains constant. Besides, PPD is also triggered by the negative bias voltage, as shown in Figure S10 (Supporting Information). The observed PPF and PPD behaviors in the ReS_2-based ferroelectric synaptic devices can be attributed to the accumulation of polarization in ferroelectric materials. When the interval time between two voltage spikes is shorter than the polarization relaxation time, the initially stimulated polarization, caused by the first spike, does not return to

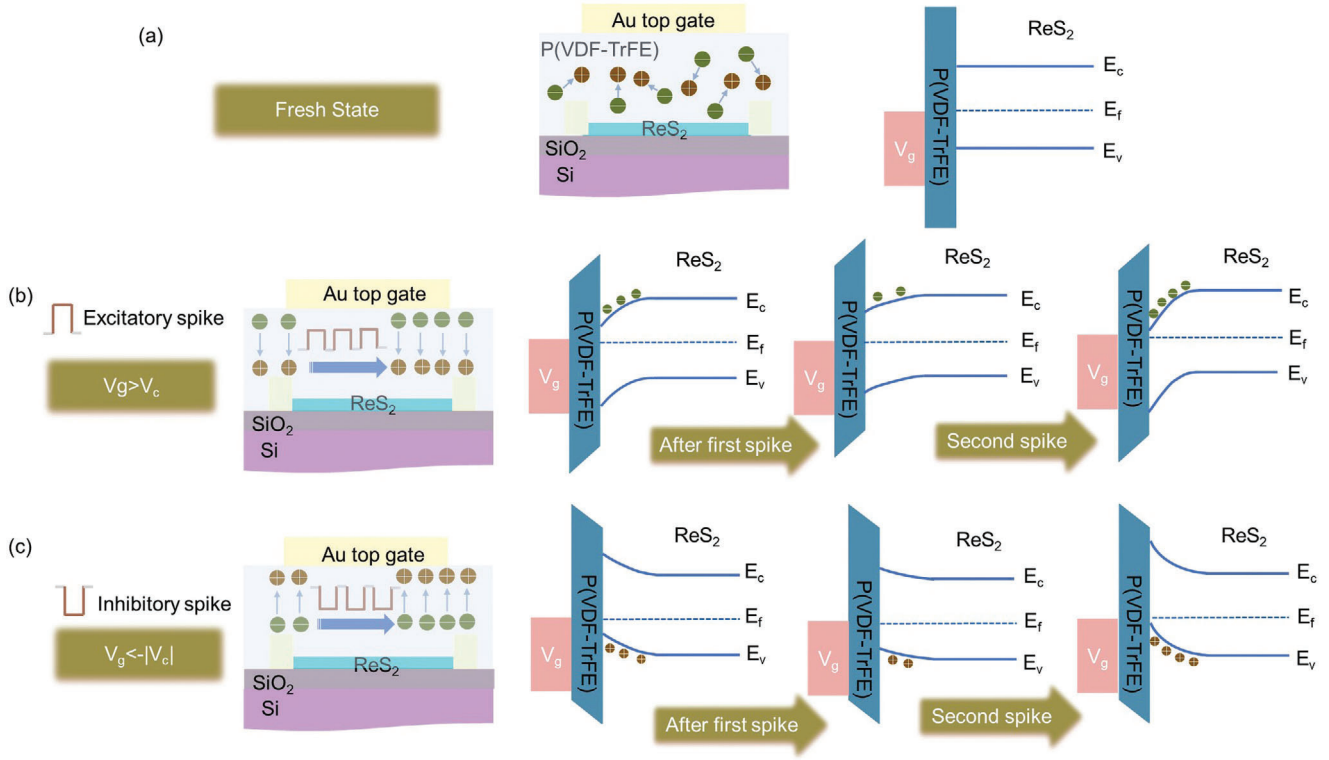

Figure 3. Working mechanism of the ferroelectric synaptic device P(VDF-TrFE)/ReS_2 under electronic mode. Dipoles distribution and energy band diagram of the ReS_2 ferroelectric transistor covered with P(VDF-TrFE) under a) fresh state, b) polarization down state, and c) polarization up state, respectively.

its original level by the time when the second spike arrives. Consequently, stronger polarization is accumulated after the second spike, resulting in an enhancement of the PSC.[43]

Synaptic plasticity can also be modulated by different temporal patterns and the frequency-dependent behaviors have an impact on information transmission between neurons.[44] In this context, Figure 2f provides further insight into the EPSC response when several positive consecutive trains with varying frequencies are applied. At elevated spike frequencies, an augmented EPSC can be observed with a prolonged decay period. Moreover, the amplitude gain, defined as (An – A1)/A1, is used to characterize the filtering property of the device. An and A1 represent the EPSC amplitude of the first and last spikes, respectively. As depicted in Figure S11 (Supporting Information), the amplitude gain increases at high frequencies, reaching up to 15% at a frequency of 4.2 Hz, which is similar to the function of high-pass filtering.

The dynamics of P(VDF-TrFE) polarization, facilitated by voltage-tunable domain wall propagation, allows for the generation of multilevel resistive states and the modulation of connection strength between pre- and post-synapses.[45] Through the application of a sequence of identical voltage pulses of ±20 V exceeding the V_c to the ferroelectric P(VDF-TrFE) gate, a progressive alteration of channel conductance states is achieved. This enables the realization of long-term potentiation (LTP) and long-term depression (LTD) processes, based on the evolution of EPSC and inhibitory postsynaptic currents (IPSC). Here, Figure 2g illustrates the reliable and repeatable emulation of LTP and LTD behaviors in P(VDF-TrFE)/ReS_2. To investigate the characteristics of LTP/LTD, we calculate realistic parameters such as linearity, cycle-to-cycle variation, and symmetry based on a single group of LTP/LTD, as depicted in Figure S12, Table S1, and Note S2 (Supporting Information). These experimental results demonstrate the effective emulation of biological synaptic behaviors in P(VDF-TrFE)/ReS_2, showcasing their potential for neuromorphic computation.

The multi-level PSC represents that synaptic weights can be integrated into an artificial neural network (ANN) for handwritten recognition. The training is performed with CrossSim platform.[46,47] Figure S13 and Note S3 (Supporting Information) present a schematic diagram consisting of a three-layer network to illustrate the input pattern recognition process. The multi-layer platform is trained on different patterns at each epoch selected from the MNIST database, and the outcome is further tested.[48] The recognition accuracy of P(VDF-TrFE)/ReS_2 synapse during 40 epochs is shown in Figure 2h. A significant increase is occurred in initial epochs, ultimately stabilizing at a saturation level of 89%. Such high accuracy is comparable to state-of-the-art nonvolatile memories.[49,50]

Figure 3 elucidates the working mechanism of ferroelectric synaptic devices P(VDF-TrFE)/ReS_2 through the band diagrams. In the fresh state, the distribution of dipoles in the ferroelectric layer is approximately random, and there is no significant energy band bending in the ReS_2 channel (Figure 3a). By applying a positive gate voltage above V_c (Figure 3b), ferroelectric dipoles become orderly arranged pointing from the gate electrode to the ReS_2 channel, and the polarization in the

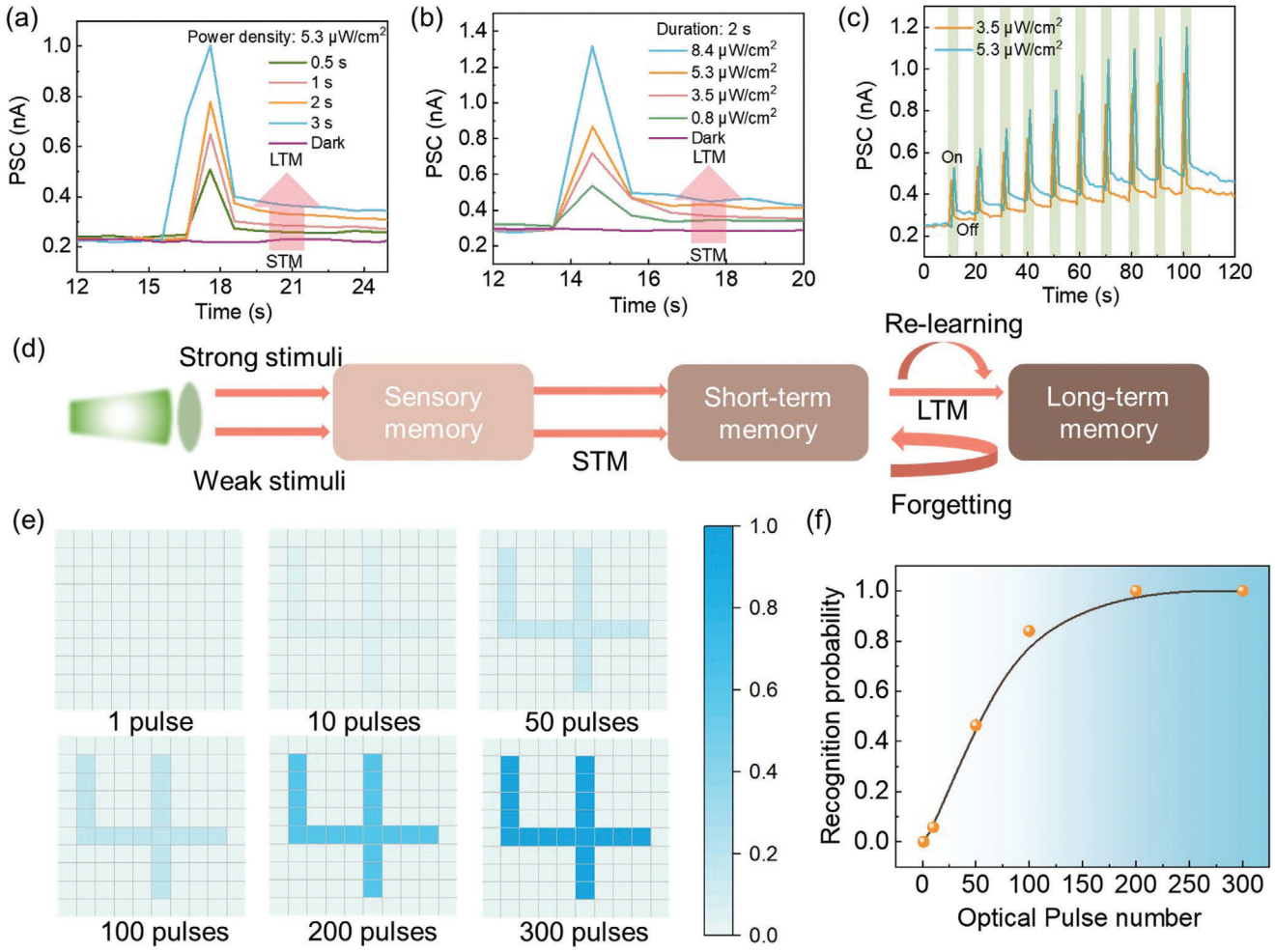

Figure 4. Optoelectronic behaviors of the artificial ferroelectric synapse and its visual memory function under 450 nm wavelength without gate voltage. a) Dependent plasticity of synaptic devices in various duration time (a) and intensities b) of light illumination under 0.1 V bias voltage. c) Light-tunable behaviors by ten consecutive light spikes under two different light intensities of 3.5 and 5.3 μW cm^{-2} with 5% duty cycle. The bias voltage is kept at 0.1 V. d) The learning–forgetting–relearning procedure is based on the above continuous optical stimulations. e) The digit '4' is mapped to the 10 × 10 array by applying a different number of light stimuli to implement the image recognition task. f) Image recognition probability results with the change of light spike numbers.

P(VDF-TrFE) layer is driven downward. Electron accumulation occurs in the ReS_2 channel. The energy band of ReS_2 at the interface bends downward while the Femic level is closer to the conductance band, which indicates the low-resistance state. Following the elimination of the electrical spike, the alignment of the ferroelectric dipoles persists, generating the nonvolatile memory functionality. Meanwhile, a gradual alteration of the polarization domains occurs as the spike pulse is continuously applied, accompanied by a notable increase of electrons within the channel region. Therefore, subsequent spikes bring with enhanced channel conductance. Such continuous evolution of ferroelectric domains can be regarded as the ferroelectric plasticity. Conversely, a negative electrical pulse induces upward polarization in the P(VDF-TrFE) polymer, depleting electrons in the ReS_2 channel, and energy-band bends upward. At this time, the Fermi level is close to the valence band and high-resistance state is demonstrated, as shown in Figure 3c. Similarly, such behavior is also featured with nonvolatile characteristic. When the inhibitory spikes are applied consecutively, the polarization domains are aligned upward gradually, thereby depleting electrons in the channel.

For biological visual systems, image pre-processing is a fundamental property of the human retina, contributing to the high-efficiency image recognition tasks. Beyond electronic operation mode, to build a neuromorphic vision system, it is imperative to study the light-tunable synaptic plasticity for perception and memory functions.[51] Also, to overcome the disadvantage of conventional artificial photoreceptors, P(VDF-TrFE)/ReS_2 optoelectronic devices can reflect light-tunable PSC states and integrate image data recognition, storage, and pre-processing within one device configuration. Thereafter, this study focuses on examining the effects of illumination conditions on PSCs.

Initially, we achieve the transition from short-term memory (STM) to long-term memory (LTM) to modulate the synaptic weight of the optoelectronic synapse by varying the amplitude and width of the light pulses. **Figure** 4a,b illustrate the PSC of the P(VDF-TrFE)/ReS_2 optoelectronic device under different

light durations (dark, 0.5, 1, 2, and 3 s) and light intensities (dark, 0.8, 3.5, 5.3, and 8.4 μW cm^{-2}) at a wavelength of 450 nm. Under the small light intensity or short light duration, the PSC increases slightly and returns to the initial level after removing optical stimuli, resembling the STM of the human brain. With an increase of light intensity or light duration time, the PSC increases gradually and decays slowly, and maintains at a higher level above the initial state, which behaves like LTM. The light-tunable behaviors can be attributed to the photo response of channel material ReS_2. PSC originates from the photogenerated carriers under illumination and the slow decay process results from the PPC effect within ReS_2, which mimics the information transmission of biological neural function.[52] Specifically, the relaxation process after light removal is prolonged due to the localized effect of trap states such as sulfur vacancy in ReS_2.[53] We also implement density functional theory (DFT) calculations on defective ReS_2 models to further elucidate that trap states are in conjunction with the generation of S vacancy. The easily formed S vacancy and the related trap states are responsible for optoelectronic synaptic behaviors and more details are shown in Figure S14 and Note S4 (Supporting Information). The PPC effect exhibits similarity with the integrated photoelectric conversion and response storage observed in the human visual system.[25]

Moreover, the learning-forgetting-relearning process is also displayed based on P(VDF-TrFE)/ReS_2 optoelectronic devices by applying several continuous light pulses, as shown in Figure 4c. On and off states of light pulses represent learning and forgetting processes, respectively. The PSC is increased during light stimulation and decays to an intermediate state after removal of optical source. Such decay signifies a slight forgetting of the acquired information within a short interval of time. The next optical stimulation represents the relearning process, and the PSC after the second pulse surpasses the initial value, indicating the consolidation of earlier information through the repeated learning process. Following all the optical stimuli, the PSC exhibits good repeatability and reaches maximum level. The current after the light irradiation can be used to demonstrate human visual forgetting curve, which approximates the exponential law[54] and the decay rate or memory duration can be modulated by different light intensities. Detailed memory retention ratio and its fitting curve can be found in Figure S15 and Note S5 (Supporting Information). We present the time-resolved response of the PSC under two different light intensities, namely 3.5 and 5.3 μW cm^{-2} in Figure 4c, and notably stronger stimuli yield a larger PSC, suggesting a higher degree of learning. The entire process is in accordance with the human memory model,[55] as shown in Figure 4d. The process of information memorization can be divided into three stages: sensory memory in the short term can be transformed into STM after learning; through repeated cycles of training, forgetting, and relearning, this information can eventually be consolidated into LTM.

Interestingly, the PSC can be modulated by optical pulse number and increases gradually with the number of stimuli. Likewise, under continuous visual stimulation, our human visual system will implement image recognition and discrimination.[56] To simulate such biological activity, an optoelectronic synaptic array is designed based on the features of a single device that will receive different numbers of optical stimuli. The data acquired from device measurements are extended to array simulations, assuming that the sensing terminal represents an ideal uniform array composed of P(VDF-TrFE)/ReS_2 optoelectronic synaptic devices. Figure 4e illustrates different numbers of optical pulses (1 s, 3.5 μW cm^{-2}) applied to the optoelectronic device, forming a visual signal for target object "4". By applying more pulses, the synaptic strength of the device is enhanced according to the time-resolved measurements (Figure S16, Supporting Information). The largest peak value of the PSC is normalized to 1. As shown in the 10 × 10 optoelectronic device array, the shape of the "4" object is difficult to distinguish from the background after the first optical pulse, indicating a relatively weak optical response at this stage. Based on the increased current response to more optical pulses, the demonstrated neuromorphic phototransistor exhibits capabilities in image recognition and memorization. Therefore, the synaptic weights and image contrast can be strengthened with an increasing number of optical pulses, bringing with a clearer representation of the object feature "4" through this image perceptual learning process.

To identify the feature maps, an ANN is constructed with 784 input neurons, 200 hidden neurons, and 10 output neurons. Note S6 (Supporting Information) illustrates the detailed method to identify feature information in the synaptic sensor array. Figure 4f demonstrates a gradual enhancement in the probability of image recognition for the digit "4" as the number of optical pulses increases. Ultimately, it reaches a saturation point, indicating the transition from being indistinguishable to visible. This application confirms the effectiveness of the neuromorphic visual system in performing image recognition tasks, including enhancing contrast and storing visual information at the sensing stage.[57,58] We further use two optical intensities to capture light and shade from different objects. Taking the light bulb as an example (Figure S17, Supporting Information), different optical intensities of 5.74 and 9.11 μW cm^{-2} are used to modulate the outline of the light bulb and the light emitted from it, respectively. When a greater number of optical pulses are inputted into the neuromorphic visual array system for light bulb and illumination recognition, both shapes can be distinguished due to the memory capability.

Power consumption is a critical concern for both electronic and optoelectronic programming modes. We calculate the energy consumption for each synaptic event. Under the optical operation, the energy consumption can be calculated as follows:

$$d\,E_{optical} = S \times P_{light} \times dt \tag{3}$$

in the above equation, S represents the active area of a single device, P denotes the optical density, and dt signifies the time duration. Whereas the energy consumed in electrical processing can be described as follows:

$$E_{electrical} = V_d \times I_{peak} \times t_{on} \tag{4}$$

where I_{peak} represents the peak current through the active channel, t_{on} signifies the time duration of the electrical pulse, and V_d denotes the source-drain voltage. The minimum energy consumption for electronic and optoelectronic programming modes are 2.7 fJ and 64 fJ, respectively, which closely approaches the biological synapse of 10 fJ.[59] The low power consumption observed can be attributed to two key factors: the high crystalline

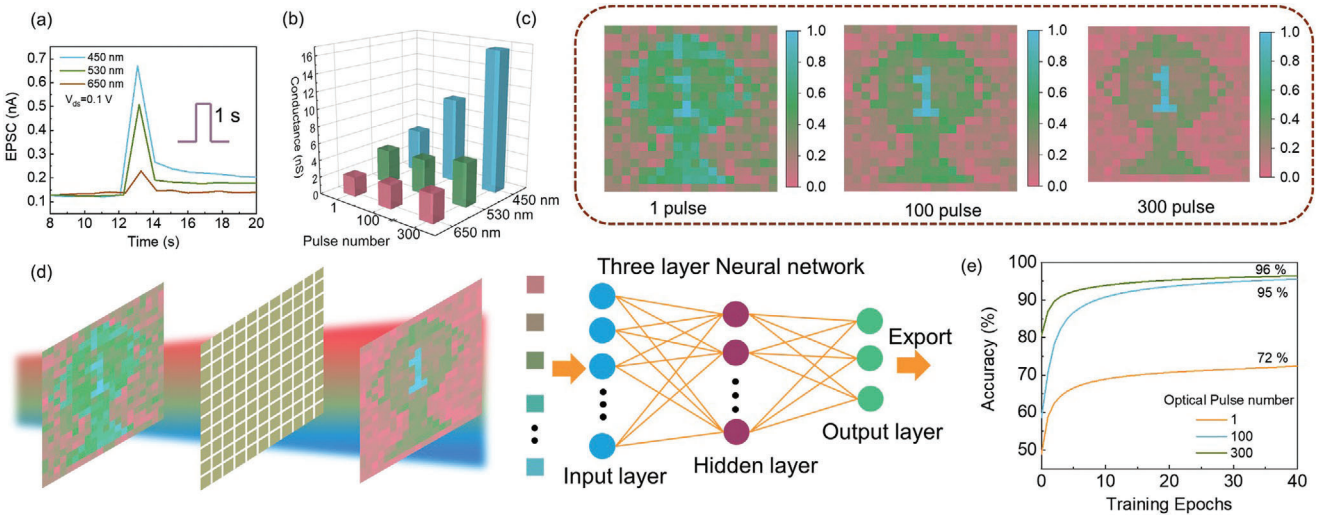

Figure 5. Simulations of information extraction based on a neuromorphic visual system with the optoelectronic array. a) The time-dependent variation of EPSC is examined under a single optical pulse with various light wavelengths. The optical pulse possesses a power density of 5.3 μW cm^{-2} and a duration lasting 1 second. b) 3D histogram image of the conductance states as a function of pulse number under three wavelengths. c) The information extraction and noise reduction processes with optical spikes number enhancement. d) Scheme of the image recognition using ANN. e) Comparisons of the image recognition rate for the three optical pulse settings.

quality of the ferroelectric copolymer P(VDF-TrFE) and the favorable interface between P(VDF-TrFE) and ReS_2. These factors collectively facilitate rapid polarization switching and efficient carriers transportation.[60] Figure S18 and Note S7 (Supporting Information) display energy consumption calculation process of single synaptic event and the outcomes are compared with other related optoelectronic synaptic works (Table S2, Supporting Information).

To achieve a versatile neuromorphic visual processing platform, in addition to perceptual learning and image recognition based on a single wavelength, we also apply the optoelectronic device array to demonstrate complicated functions of multi-wavelength information extraction and surrounding noise signal reduction simultaneously.

The light-induced current is analyzed based on different wavelengths, as illustrated in **Figure** 5a. Three specific wavelengths, namely 450 nm, 530 nm, and 650 nm are employed, which correspond to the primary colors of blue, green, and red. These wavelengths are used to stimulate the optoelectronic devices at a fixed optical intensity of 5.3 μW cm^{-2} and a constant pulse duration of 1 s. The PSC gradually increases as the wavelengths transition from 650 nm to 450 nm. This finding suggests that the wavelength-dependent photo response displays a high sensitivity to blue source illumination. Such behavior can be attributed to the special optical absorption properties of ReS_2 (Figure S19, Supporting Information), eliminating the need for other optical filters or complex circuits.[61,62] We further investigate the light-induced conductance states under different pulse numbers with three wavelengths (Figure 5b). As light pulses number increases, the conductance of blue illumination become much higher and more pronounced compared to green or red sources. Detailed time-resolved EPSC variations for the pulse numbers of 100 and 300 are displayed in Figure S20 (Supporting Information). By leveraging the wavelength-sensing capabilities for blue light and the heightened sensitivity achieved through increasing the number of optical pulses, the proposed visual sensor array has the potential to effectively extract blue information. As shown in Figure 5c, the background section, the outline of the trophy, and the digit on the trophy are corresponded to the red, green, and blue colors in the original image. The relationship between optical wavelength and its position in the 20 × 20 optoelectronic device array is defined based on the original image. Each optoelectronic device in the array is assumed to be illuminated with three different pulse numbers according to above relationship. Optical-induced EPSCs are extracted from experimental results involving 1 pulse, 100 pulses, and 300 pulses. Additionally, the normally distributed noise signals are taken into consideration for image pre-processing. All the current responses and the undesired signals are normalized from 0 to 1 in each optoelectronic array mapping. With an increase in the number of pulses, the blue number on the trophy becomes more prominent, aligning with the experimental results presented in Figure 5b, while the noise signals become less noticeable (Figure 5c). The finding suggests that by increasing the pulse number, the distinction between the blue features and other features can be intensified and the optoelectronic sensor array can effectively recognize blue targets while minimizing signals from other sources. Similar to the visual cortex, it records information that is crucial for brain while suppressing irrelevant parts or noises.[26]

To explore the concept of bio-vision-inspired neuromorphic computation, a simulated visual system has been developed. This system includes the demonstrated neuromorphic vision sensor array and an ANN. After the outline of the blue digit on the trophy becomes highlighted while the background noise signals are depressed through the optoelectronic array. The preprocessed image is subsequently fed into the neural network for image training and recognition, as shown in Figure 5d. The detailed operation mechanism of the simulated visual system and noise generation method are shown in Note S8 (Supporting Information). Figure 5e illustrates the recognition rate of neuromorphic visual

systems while considering noises. In the initial state, noticeable differences in recognition accuracy are observed among the three optical pulse settings. For one optical pulse illumination, the image recognition accuracy after 40 epochs is merely 72%, indicating that the network struggles to identify critical information displayed on the trophy due to surrounding interference. However, through image pre-processing via the optoelectronic array, the recognition rate significantly improves to 95% and 96% for 100 optical pulses and 300 optical pulses, respectively, after 40 training epochs. It is imperative to acknowledge that the acquisition of 300 pulses requires a considerable amount of time. However, it is noteworthy that the precision attained with 100 pulses at ≈95% accuracy level is comparable to that achieved with 300 pulses while requiring a significantly shorter duration. Therefore, the redundant signals have been reduced dramatically and previously unrecognizable information can be accurately extracted by our neuromorphic vision system in conjunction with the neural network.

The aforementioned results emphasize the versatile capabilities of the demonstrated sensor array in image recognition, memorization, and pre-processing based on light-tunable synaptic behaviors. In addition to its ability to perform single wavelength recognition, the P(VDF-TrFE)/ReS_2 optoelectronic array can effectively extract essential information from complicated colored images while simultaneously reducing noise signals. It further approaches a more realistic emulation of the human visual system performed by retinal cells.

3. Conclusion

In conclusion, an artificial optoelectronic synaptic device based on P(VDF-TrFE)/ReS_2 has been successfully designed that can act as a sensory component to electrical and optical stimuli and emulate versatile biological behaviors through ferroelectric nonvolatile switching effect. The optical synapses array, with its light-tunable plasticity, allows for the implementation of learning processes including image recognition and contrast enhancement. Furthermore, the entire array can be utilized for multi-wavelength recognition in noisy environments, facilitating the information extraction while reducing noise signals. To address concerns regarding hardware and power consumption, we have constructed a neural network integrating the proposed optoelectronic devices array. Through the redundant information reduction and the target extraction processes, the image pre-processing efficiency has been increased from 72% to 96%. Our study underscores the advantages of utilizing ferroelectric optoelectronic synapses in artificial visual platforms, as they offer simplified device structures and expedite the advancement of in-sensor neuromorphic computation.

4. Experimental Section

Device Fabrication: First, Ti/Au (5 nm/25 nm) metal electrodes were prepared on p-Si/SiO_2 (285 nm) substrates with standard lithography technique and electron beam deposition. 2D ReS_2 flakes were mechanically exfoliated onto the polydimethylsiloxane (PDMS) supports with blue tape. The ReS_2 flakes were identified on the PDMS by the optical microscope, and then interested ones were selected for further dry transfer process. The P(VDF-TrFE) (70:30 in mol %) thin films (≈300 nm in thickness) as dielectric layers were made by the spin-coating process. The detailed parameters for the spin-coating were 400 rpm for 10 s and 3000 rpm for 40 s. The P(VDF-TrFE)/ReS_2 structures were annealed at 135 °C in the vacuum for 2 h. Finally, a semi-transparent Au electrode of 10 nm as the top metal electrode was transferred through Polyvinyl butyral (PVB) films. Then, the whole device was immersed into the ethyl alcohol solution for half an hour under 45 °C to dissolve the PVB film without damage to the P(VDF-TrFE) copolymer and the whole device structure.

Characterization and Measurement: Raman investigations of ReS_2 flakes were carried out with high-resolution confocal μ-Raman microscopes (WITEC alpha300 R) equipped with 532 nm laser sources. The thicknesses of few-layer ReS_2 films were investigated using a commercial atomic force microscope (Asylum Research MFP-3D) and PFM measurements were carried under DART PFM mode. The P–E hysteresis loops were measured with a ferroelectric analysis instrument of The TF Analyzer 3000, manufactured by aixACCT. The XRD of P(VDF-TrFE) films were examined using X-ray diffraction (Rigaku SmartLab, 9 kW) with Cu Kα radiation (λ = 1.5406Å). The top-gate FeFETs were tested by the semiconductor analyzer (Keithley 4200) in a probe station (Lake Shore CRX-6.5K) under vacuum and room-temperature environment. The 450 nm, 530 nm, and 650 nm monochromatic LED lights were employed as the light source for the optical mode measurements. A power meter (SANWA, LP1) was used to calibrate the light intensity. To perform time-dependent optical response measurements, the LED frequency was modulated by a signal function generator.

Supporting Information

Supporting Information is available from the Wiley Online Library or from the author.

Acknowledgements

This work was supported by the National Natural Science Foundation of China (no. 52233014), Research Grants Council of Hong Kong (PolyU SRFS 2122–5S02), and PolyU Projects (1-CE0H, Q-CDBD,1-W22S and 1-CD7V).

Conflict of Interest

The authors declare no conflict of interest.

Data Availability Statement

The data that support the findings of this study are available from the corresponding author upon reasonable request.

Keywords

2D materials, image pre-processing, neuromorphic visual platform, optoelectronic synapses, P(VDF-TrFE) ferroelectric transistors

Received: January 3, 2024
Revised: February 20, 2024
Published online: March 10, 2024

[1] T. Gollisch, M. Meister, *Neuron* **2010**, *65*, 150.
[2] G. Wu, X. Zhang, G. Feng, J. Wang, K. Zhou, J. Zeng, D. Dong, F. Zhu, C. Yang, X. Zhao, *Nat. Mater.* **2023**, *22*, 1499.

[3] F. Zhou, Z. Zhou, J. Chen, T. H. Choy, J. Wang, N. Zhang, Z. Lin, S. Yu, J. Kang, H.-S. P. Wong, *Nat. Nanotechnol.* **2019**, *14*, 776.
[4] N. Li, S. Zhang, Y. Peng, X. Li, Y. Zhang, C. He, G. Zhang, *Adv. Funct. Mater.* **2023**, *33*, 2305589.
[5] L. Mennel, J. Symonowicz, S. Wachter, D. K. Polyushkin, A. J. Molina-Mendoza, T. Mueller, *Nature* **2020**, *579*, 62.
[6] X. Wang, Y. Zong, D. Liu, J. Yang, Z. Wei, *Adv. Funct. Mater.* **2023**, *33*, 2213894.
[7] A. Dodda, D. Jayachandran, S. Subbulakshmi Radhakrishnan, A. Pannone, Y. Zhang, N. Trainor, J. M. Redwing, S. Das, *ACS Nano* **2022**, *16*, 20010.
[8] J. Yu, X. Yang, G. Gao, Y. Xiong, Y. Wang, J. Han, Y. Chen, H. Zhang, Q. Sun, Z. L. Wang, *Sci. Adv.* **2021**, *7*, eabd9117.
[9] Z. Zhang, S. Wang, C. Liu, R. Xie, W. Hu, P. Zhou, *Nat. Nanotechnol.* **2022**, *17*, 27.
[10] F. Liao, Z. Zhou, B. J. Kim, J. Chen, J. Wang, T. Wan, Y. Zhou, A. T. Hoang, C. Wang, J. Kang, *Nat. Electron.* **2022**, *5*, 84.
[11] Y. Pei, L. Yan, Z. Wu, J. Lu, J. Zhao, J. Chen, Q. Liu, X. Yan, *ACS Nano* **2021**, *15*, 17319.
[12] B. Cai, Y. Huang, L. Tang, T. Wang, C. Wang, Q. Sun, D. W. Zhang, L. Chen, *Adv. Funct. Mater.* **2023**, *33*, 2306272.
[13] S. M. Kwon, S. W. Cho, M. Kim, J. S. Heo, Y. H. Kim, S. K. Park, *Adv. Mater.* **2019**, *31*, 1906433.
[14] Q.-B. Zhu, B. Li, D.-D. Yang, C. Liu, S. Feng, M.-L. Chen, Y. Sun, Y.-N. Tian, X. Su, X.-M. Wang, *Nat. Commun.* **2021**, *12*, 1798.
[15] T. Li, J. Miao, X. Fu, B. Song, B. Cai, X. Ge, X. Zhou, P. Zhou, X. Wang, D. Jariwala, *Nat. Nanotechnol.* **2023**, *18*, 1303.
[16] G. Cao, P. Meng, J. Chen, H. Liu, R. Bian, C. Zhu, F. Liu, Z. Liu, *Adv. Funct. Mater.* **2021**, *31*, 2005443.
[17] C. Jo, J. Kim, J. Y. Kwak, S. M. Kwon, J. B. Park, J. Kim, G. S. Park, M. G. Kim, Y. H. Kim, S. K. Park, *Adv. Mater.* **2022**, *34*, 2108979.
[18] J. Lee, B. H. Jeong, E. Kamaraj, D. Kim, H. Kim, S. Park, H. J. Park, *Nat. Commun.* **2023**, *14*, 5775.
[19] L. Lv, F. Zhuge, F. Xie, X. Xiong, Q. Zhang, N. Zhang, Y. Huang, T. Zhai, *Nat. Commun.* **2019**, *10*, 3331.
[20] F. Guo, W. F. Io, Z. Dang, R. Ding, S.-Y. Pang, Y. Zhao, J. Hao, *Mater. Horiz.* **2023**, *10*, 3719.
[21] E. Liu, Y. Fu, Y. Wang, Y. Feng, H. Liu, X. Wan, W. Zhou, B. Wang, L. Shao, C.-H. Ho, *Nat. Commun.* **2015**, *6*, 6991.
[22] D. Xie, K. Yin, Z.-J. Yang, H. Huang, X. Li, Z. Shu, H. Duan, J. He, J. Jiang, *Mater. Horiz.* **2022**, *9*, 1448.
[23] S. Li, B. Li, X. Feng, L. Chen, Y. Li, L. Huang, X. Fong, K.-W. Ang, *npj 2D Mater. Appl.* **2021**, *5*, 1.
[24] Y. Chen, Y. Kang, H. Hao, X. Xie, J. Zeng, T. Xu, C. Li, Y. Tan, L. Fang, *Adv. Funct. Mater.* **2023**, *33*, 2209781.
[25] S. Seo, J. J. Lee, R. G. Lee, T. H. Kim, S. Park, S. Jung, H. K. Lee, M. Andreev, K. B. Lee, K. S. Jung, *Adv. Mater.* **2021**, *33*, 2102980.
[26] R. Yu, L. He, C. Gao, X. Zhang, E. Li, T. Guo, W. Li, H. Chen, *Nat. Commun.* **2022**, *13*, 7019.
[27] Z. Dang, F. Guo, Z. Wu, K. Jin, J. Hao, *Adv. Phys. Res.* **2023**, *2*, 2200038.
[28] Y. R. Lee, T. Q. Trung, B.-U. Hwang, N.-E. Lee, *Nat. Commun.* **2020**, *11*, 2753.
[29] M. Guo, J. Jiang, J. Qian, C. Liu, J. Ma, C. W. Nan, Y. Shen, *Adv. Sci.* **2019**, *6*, 1801931.
[30] H. L. Park, H. Kim, D. Lim, H. Zhou, Y. H. Kim, Y. Lee, S. Park, T. W. Lee, *Adv. Mater.* **2020**, *32*, 1906899.
[31] Q. Chen, Y. Zhang, S. Liu, T. Han, X. Chen, Y. Xu, Z. Meng, G. Zhang, X. Zheng, J. Zhao, *Adv. Intel. Syst.* **2020**, *2*, 2000122.
[32] F. Zhang, C. Li, Z. Li, L. Dong, J. Zhao, *Microsyst. Nanoeng.* **2023**, *9*, 16.
[33] A. E. Pereda, *Nat. Rev. Neurosci.* **2014**, *15*, 250.
[34] D. A. Chenet, B. Aslan, P. Y. Huang, C. Fan, A. M. Van Der Zande, T. F. Heinz, J. C. Hone, *Nano Lett.* **2015**, *15*, 5667.
[35] T. Furukawa, *Ph. Transit.: A Multinatl. J.* **1989**, *18*, 143.
[36] S. Wu, Y. Chen, X. Wang, H. Jiao, Q. Zhao, X. Huang, X. Tai, Y. Zhou, H. Chen, X. Wang, *Nat. Commun.* **2022**, *13*, 3198.
[37] M. Si, A. K. Saha, S. Gao, G. Qiu, J. Qin, Y. Duan, J. Jian, C. Niu, H. Wang, W. Wu, *Nat. Electron.* **2019**, *2*, 580.
[38] G. Nazir, M. A. Rehman, M. F. Khan, G. Dastgeer, S. Aftab, A. M. Afzal, Y. Seo, J. Eom, *ACS Appl. Mater. Interfaces* **2018**, *10*, 32501.
[39] E. Liu, M. Long, J. Zeng, W. Luo, Y. Wang, Y. Pan, W. Zhou, B. Wang, W. Hu, Z. Ni, *Adv. Funct. Mater.* **2016**, *26*, 1938.
[40] H. K. Li, T. Chen, P. Liu, S. Hu, Y. Liu, Q. Zhang, P. S. Lee, *J. Appl. Phys.* **2016**, *119*, 244505.
[41] E. S. Fortune, G. J. Rose, *Trends Neurosci.* **2001**, *24*, 381.
[42] Y. H. Liu, L. Q. Zhu, P. Feng, Y. Shi, Q. Wan, *Adv. Mater.* **2015**, *27*, 5599.
[43] Z. Dang, F. Guo, H. Duan, Q. Zhao, Y. Fu, W. Jie, K. Jin, J. Hao, *Nano Lett.* **2023**, *23*, 6752.
[44] H. Markram, A. Gupta, A. Uziel, Y. Wang, M. Tsodyks, *Neurobiol. Learn. Mem.* **1998**, *70*, 101.
[45] Q. Xia, J. J. Yang, *Nat. Mater.* **2019**, *18*, 309.
[46] E. J. Fuller, F. E. Gabaly, F. Léonard, S. Agarwal, S. J. Plimpton, R. B. Jacobs-Gedrim, C. D. James, M. J. Marinella, A. A. Talin, *Adv. Mater.* **2017**, *29*, 1604310.
[47] Z.-D. Luo, S. Zhang, Y. Liu, D. Zhang, X. Gan, J. Seidel, Y. Liu, G. Han, M. Alexe, Y. Hao, *ACS Nano* **2022**, *16*, 3362.
[48] C. S. Yang, D. S. Shang, N. Liu, E. J. Fuller, S. Agrawal, A. A. Talin, Y. Q. Li, B. G. Shen, Y. Sun, *Adv. Funct. Mater.* **2018**, *28*, 1804170.
[49] F.-S. Yang, M. Li, M.-P. Lee, I.-Y. Ho, J.-Y. Chen, H. Ling, Y. Li, J.-K. Chang, S.-H. Yang, Y.-M. Chang, *Nat. Commun.* **2020**, *11*, 2972.
[50] T. Zhou, X. Lin, J. Wu, Y. Chen, H. Xie, Y. Li, J. Fan, H. Wu, L. Fang, Q. Dai, *Nat. Photonics* **2021**, *15*, 367.
[51] N. Li, C. He, Q. Wang, J. Tang, Q. Zhang, C. Shen, J. Tang, H. Huang, S. Wang, J. Li, *Nano Res.* **2022**, *15*, 5418.
[52] D. Kumar, H. Li, U. K. Das, A. M. Syed, N. El-Atab, *Adv. Mater.* **2023**, *35*, 2300446.
[53] J. Jiang, C. Ling, T. Xu, W. Wang, X. Niu, A. Zafar, Z. Yan, X. Wang, Y. You, L. Sun, *Adv. Mater.* **2018**, *30*, 1804332.
[54] J. Meng, T. Wang, H. Zhu, L. Ji, W. Bao, P. Zhou, L. Chen, Q.-Q. Sun, D. W. Zhang, *Nano Lett.* **2021**, *22*, 81.
[55] T. Ohno, T. Hasegawa, T. Tsuruoka, K. Terabe, J. K. Gimzewski, M. Aono, *Nat. Mater.* **2011**, *10*, 591.
[56] G. Wallis, E. T. Rolls, *Prog. Neurobiol.* **1997**, *51*, 167.
[57] W. Du, C. Li, Z. Long, Y. Huang, L. Luo, J. Zou, J. Wu, *IEEE Electron Device Lett.* **2021**, *42*, 1810.
[58] T. Ahmed, S. Kuriakose, E. L. Mayes, R. Ramanathan, V. Bansal, M. Bhaskaran, S. Sriram, S. Walia, *Small* **2019**, *15*, 1900966.
[59] C. Zhang, S. Wang, X. Zhao, Y. Yang, Y. Tong, M. Zhang, Q. Tang, Y. Liu, *Adv. Funct. Mater.* **2021**, *31*, 2007894.
[60] Q. Li, T. Wang, Y. Fang, X. Hu, C. Tang, X. Wu, H. Zhu, L. Ji, Q.-Q. Sun, D. W. Zhang, *Nano Lett.* **2022**, *22*, 6435.
[61] H.-X. Zhong, S. Gao, J.-J. Shi, L. Yang, *Phys. Rev. B* **2015**, *92*, 115438.
[62] M. N. Tahir, A. Yella, J. K. Sahoo, F. Natalio, U. Kolb, F. Jochum, P. Theato, W. Tremel, *Isr. J. Chem.* **2010**, *50*, 500.